Journal of Applied Electrochemistry **30**: 575–584, 2000.

Prediction of electrode shape change involving convection, diffusion and migration by the boundary element method

Z.H. QIU and H. POWER*
Wessex Institute of Technology, Southampton SO40 7AA, Great Britain
*(*Also at: Instituto de Mecánica de Fluídos, Universidad Central Venezuela, Caracas, Venezuela)*

Received 3 September 1998; accepted in revised form 3 September 1999

Key words: BEM numerical solution, electrodeposition growth

Abstract

A boundary element numerical scheme is developed to solve the problem of electrode shape change in an electrochemical process involving convection, diffusion and migration. Particular attention is paid to the role of each mechanism in determining the pattern of deposition. A uniform B-spline function is employed to define the shape of the electrode at each time step. An adaptive scheme is developed to generate the internal cells required in the BEM formulation to deal with the non-constant convection and nonlinear terms of the problem. Several tests are carried out to assess the proposed method.

List of symbols

c_k	concentration of species k (mol m^{-3})
D_k	diffusion coefficient of species k (m^2 s^{-1})
F	Faraday constant (C mol^{-1})
i^*	exchange current density (A m^{-2})
J	current density (A m^{-2})
J_{lim}	limiting current density (A m^{-2})
N_k	flux density of species k (mol m^{-2} s^{-1})
Pe	Péclet number
u_k	mechanical mobility of species k (m^2 mol J^{-1} s^{-1})
U	electrical potential (V)
∇U	electrical field (V m^{-1})
v	velocity of the solvent (m s^{-1})
V	applied voltage (V)
R	gas constant (J mol^{-1} K^{-1})
T	absolute temperature (K)
x, y	cartesian coordinates (m)
z_k	charge number of species k

Greek letters

α	transfer coefficient
ε	dielectric constant (C^2 J^{-2} m^{-1})
ρ	electrolyte density (kg m^{-3})
μ	electrolyte viscosity (kg m^{-1} s^{-1})

Subscripts

a	anode
c	cathode
k	species k

1. Introduction

Uniform electrodeposition of coatings is generally achieved when the current density is evenly distributed over the electrode surface. A major problem in practical electrochemical processes is the simultaneous effects of many complex interacting phenomena. In their most general form, the equations describing mass and charge transport in electrochemical systems are complicated because the flow itself is influenced by mechanical and electrical forces of all components. In many practical cases the solution contains a large amount of solvent, which does not contribute to the reactions. In such condition it can be assumed that the fluid flow is not influenced by the motion of the charged species (dilute solution model), consequently the fluid motion can be obtained independently of the electrochemical process, and the governing equations describing the combined mass and charge transport of reacting species can then be solved. Yet, when mass transport can be neglected, the equations describing the current density distribution reduce to a Laplace equation (diffusion model); in this condition, the variation of ion concentrations is neglected.

There are several reliable numerical schemes in the literature for the solution of the Laplace equation. Not surprisingly, there are a substantial number of publications on the numerical simulation of current distribution problems described by the diffusion model. However, it is known that mass transfer of reacting species has to be considered in several practical cases (consider [1, 2]) where the potential model fails. Numerical solution of the dilute solution model based upon classical domain formulations such as orthogonal functions, finite ele-

ments, differences and volumes have been successfully applied [3–6], but only few of these works consider multiple ions solutions [4]. Recently, Qui et al. [7, 8] developed a highly accurate boundary element scheme for solving two-dimensional electrochemical problems involving diffusion, convection and migration of several ions in a dilute solution, without taking electrodeposition into consideration.

Due to the boundary nature of the approach, the boundary elements method (BEM) is in principle ideal to simulate moving boundary problems, as is the case of the electrodeposition process. The main objective of the present work is to extend our previous BEM formulation [7] to solve problems of electrode shape change involving the effects of diffusion, convection and migration. The added difficulties of the present work lie on the moving boundary nature of the problem due to the deposition process. For more details about the accuracy of the proposed numerical scheme to simulate current density distributions controlled by diffusion, convection and migration [8], where comparisons with analytical solutions, other numerical schemes and experiments are reported.

There is a considerable number of papers in the literature on the numerical solution of electrodeposition problems (e.g., [9–14]), most of them in terms of the potential theory. Amongst there, the following are worth of special attention: Deconinck and collaborators [10–12] simulated the electrode shape change in electrodeposition process by employing a diffusion model, with special attention paid to the electrode variation in the vicinity of the adjacent insulator where a singularity is expected to occur. They pointed out that the angle of incidence between an electrode and an adjacent insulator becomes a right angle as the evolution progresses; this observation has been confirmed by several experiments. More recently, Huang and Hibbert [15] developed a one-dimensional model for the simulation of electrode-position including diffusion, convection and constant migration field, and Huang and Hibbert [16] presented a probability approach based upon a modified diffusion limited aggregation model to predict the pattern formation of electrodeposition process in a two-dimensional cell with constant fluid velocity and electrical fields. The authors of [15, 16] assumed that the charged layer is very narrow and the cell is quasi-neutral, so the electrical field gradient can be ignored.

Although several researchers have published results on electrode shape changes, simulations of the changing current distribution and resulting electrodeposition for the problems involving diffusion, convection and migration have hardly appeared.

In our numerical examples, particular attention will be paid to the role of each of these mechanisms, that is, diffusion, convection and migration, in determining the final shape of the deposition patterns at the cathode. In the literature, there is no general classification for the description of the deposition features, which may develop in an electrodeposition process. Even more difficult is the definition of conditions which may lead to the various types of deposition forms. Calusaru [17, 18] and Atanasiu and Calusaru [19] showed that there are at least three ranges of overpotential, which can be determined from studies of the deposited structure: (i) compact metal, (ii) rough deposition, and (iii) true powder. It is also known that all metals which can be electrodeposited exhibit a tendency to appear in the form of powder at current densities larger than a certain critical value (for more details see Pavlovic et al. [20]).

2. Governing equations

For a dilute solution in a unionised solvent at constant pressure and temperature, the vector flux density of each ionic species k is given by [21]

$$\boldsymbol{N}_k = -z_k F u_k c_k \nabla U - D_k \nabla c_k + \mathbf{v} c_k \tag{1}$$

where c_k is the molar concentration of ion k, ∇c_k the concentration gradient, D_k the diffusion coefficient, u_k the mechanical mobility, z_k the charge number, ∇U the electrical field, $\mathbf{v}$ the velocity of the solvent, and F the Faraday constant ($F = 96\,487$ C mol^{-1}).

The three terms on the right-hand side of the equation describe the effects of migration, diffusion and convection, respectively. The total charge per mole ion is its charge number multiplied by the constant $z_k F$, and the current density is hence the flux of the ion multiplied by $z_k F$. For all species, we have

$$\boldsymbol{J} = F \sum_k z_k \boldsymbol{N}_k \tag{2}$$

The material balance for a minor component in an electrolyte can be expressed by

$$\frac{\partial c_k}{\partial t} = -\nabla \cdot \boldsymbol{N}_k + R_k \tag{3}$$

with $\partial c_k / \partial t$ being the accumulation of species k, $\nabla \cdot \boldsymbol{N}_k$ the difference between the input and the output and R_k the production rate of ion k due to homogeneous chemical reaction at the bulk of the solution. In electrochemical systems, reactions are frequently restricted to electrode surfaces, in which case R_k can be considered as zero.

Equations 1 and 3 are equivalent to the following system of equations:

$$\frac{\partial c_k}{\partial t} + \mathbf{v} \cdot \nabla c_k = z_k F \nabla \cdot (u_k c_k \nabla U) + \nabla \cdot (D_k \nabla c_k) + R_k \tag{4}$$

$$\nabla \cdot \left\{ -F^2 \sum_k z_k^2 u_k c_k \nabla U - F \sum_k z_k D_k \nabla c_k \right\} = 0 \tag{5}$$

where Equation 5 was obtained by considering conservation of charge and the condition of electroneutrality

$$\sum_k z_k c_k = 0 \tag{6}$$

The above system of equations describes the transport of mass and charge in dilute electrochemical solutions. Even in the simple case of an infinite dilute solution, a complex set of coupled partial differential equations has to be dealt with. With prescribed convective velocity, Equations 4 to 6 can be solved to get the unknowns U and c_k.

3. Numerical formulation

3.1. *Mathematical model*

For two-dimensional steady-state conditions, and assuming that the coefficients u_k, z_k and D_k are all constant, Equations 4 and 5 can be expressed in the form:

$$D_k\nabla^2 c_k - \left(v_x - Fz_k u_k \frac{\partial}{\partial x}U\right)\frac{\partial}{\partial x}c_k - \left(v_y - Fz_k u_k \frac{\partial}{\partial y}U\right)\frac{\partial}{\partial y}c_k = -\left(Fz_k u_k \nabla^2 U\right)c_k \tag{7}$$

and

$$\left(\sum_k z_k^2 u_k c_k\right)\nabla^2 U + \left(\sum_k z_k^2 u_k \frac{\partial}{\partial x}c_k\right)\frac{\partial}{\partial x}U + \left(\sum_k z_k^2 u_k \frac{\partial}{\partial y}c_k\right)\frac{\partial}{\partial y}U = -\frac{1}{F}\sum_k z_k D_k \nabla^2 c_k \tag{8}$$

In the present work the above system of equations can be used as the governing equations of the problem under consideration. This is due to the quasi-static character of the phenomena, consequence of the difference between the characteristic time scale of the chemical reactions, the deposition and flow processes.

For the purpose of deriving the numerical algorithm employing the boundary element method, the velocity field is divided into an average and a perturbation, and the fundamental solution of the diffusion–convection equation for constant velocity is applied. The perturbation velocity and migration terms are included through a domain discretization. After dividing the velocity field into average and perturbation, Equation 7 is rewritten in the form

$$D_k\nabla^2 c_k - \bar{v}_x\frac{\partial}{\partial x}c_k - \bar{v}_y\frac{\partial}{\partial y}c_k = P_{cx_k}\frac{\partial}{\partial x}c_k + P_{cy_k}\frac{\partial}{\partial y}c_k + C_{xy_k}c_k \tag{9}$$

with

$$P_{cx_k}(x,y) = P_x - K_k\frac{\partial}{\partial x}U$$

$$P_{cy_k}(x,y) = P_y - K_k\frac{\partial}{\partial y}U$$

$$C_{xy_k}(x,y) = -K_k\nabla^2 U$$

$$K_k = Fz_k u_k$$

Similarly, Equation 8 is rewritten in the form:

$$\nabla^2 U - \bar{v}_{ux}\frac{\partial}{\partial x}U - \bar{v}_{uy}\frac{\partial}{\partial y}U = P_{ux}\frac{\partial}{\partial x}U + P_{uy}\frac{\partial}{\partial y}U + U_{xy} \tag{10}$$

with

$$v_{ux}(x,y) = -\left(\sum_k z_k^2 u_k \frac{\partial}{\partial x}c_k\right)\Big/\left(\sum_k z_k^2 u_k c_k\right)$$

$$v_{uy}(x,y) = -\left(\sum_k z_k^2 u_k \frac{\partial}{\partial y}c_k\right)\Big/\left(\sum_k z_k^2 u_k c_k\right)$$

$$U_{xy}(x,y) = -\left(\sum_k z_k D_k \nabla^2 c_k\right)\Big/\left(F\sum_k z_k^2 u_k c_k\right)$$

The fundamental solution of the two-dimensional steady-state diffusion–convection equation with constant velocity field

$$D\nabla^2 c - \bar{v}_x\frac{\partial c}{\partial x} - \bar{v}_y\frac{\partial c}{\partial y} = 0$$

is of the form

$$c^*(\xi,\chi) = \frac{1}{2\pi D}\mathrm{e}^{-(\bar{\mathbf{v}}\cdot\mathbf{r})/2D}K_0\left(\frac{|\bar{\mathbf{v}}|r}{2}\right)$$

By employing the above fundamental solution and Green's second identity, when the source point is inside the domain, Equation 9 can be transformed into the following integral representational formula:

$$c_k(\xi) - D_k\int_\Gamma c_k^*(\xi,\chi)q(\chi)\mathrm{d}\Gamma(\chi) + D_k\int_\Gamma q_k^*(\xi,\chi)c_k(\chi)\mathrm{d}\Gamma(\chi) + \int_\Gamma c_k^*(\xi,\chi)\bar{v}_n(\chi)c_k(\chi)\mathrm{d}\Gamma(\chi) = -\int_\Omega b_k c_k^*(\xi,\chi)\mathrm{d}\Omega(\chi) \tag{11}$$

in which

$$b_k = P_{cx_k}(\partial c_k/\partial x) + P_{cy_k}(\partial c_k/\partial y) + C_{xy_k}c_k$$

For Equation 10, the integral representational formula has a similar form. A BEM algorithm to solve the above system of integral equations has been described in detail in our previous papers [7, 8]. With the above numerical scheme, we are now able to simulate the electrode shape change in the electrodeposition process by employing Faraday's law, in which the relationship between the

electrode shape change and the local current density is described.

3.2. *Electrode shape change*

Since electrodeposition is a Faraday's charge-transfer reaction, the rate of deposition depends upon the current density. In the absence of any interfering reaction, the relationship between the deposition rate and the current density is given by Faraday's law in its local form [21]:

$$\frac{\mathrm{d}h}{\mathrm{d}t} = \sum_l \frac{M_l}{z_l F \rho_l} \boldsymbol{J}_l \cdot \boldsymbol{n} \tag{12}$$

with $\mathrm{d}h/\mathrm{d}t$ being the thickness variation at a point i along the normal direction, $\boldsymbol{J}_l$ the partial current density of reduction of ion l, M_l the molecular weight, and ρ_l the specific weight. At each moment, the electric potential and the concentration of each ion have to satisfy Equations 4–6 including the boundary conditions, while the boundary contour at the electrodes changes with time. In some practical cases there can be a difference between the value predicted by Equation 12, and the observed measurements of reaction processes. This is due to the possible presence of other reactions than metal deposition of removal, as can be gas evolution, that will be neglected in the present work.

The simplest way to solve the above evolution equation is to replace the differential by a forward finite difference, hence Equation 12 becomes

$$h_i^{n+1} = h_i^n + \Delta t \left(\sum_l \lambda_l \boldsymbol{J}_l^i \cdot \boldsymbol{n}_i \right) \tag{13}$$

$$\lambda = \frac{M_l}{z_l F \rho_l}$$

with $h_i^0 = 0$. This is the classical Euler method, which is in fact the integration of the first order Taylor expansion of the real solution. At each time step n, the thickness variation is obtained from the above equation, with the current density at each nodal point obtained by solving the governing equations for the electrochemical process. The corresponding coordinates of the new electrode shape, at time step $n+1$, are

$$x_i^{n+1} = x_i^n + n_x h_i^{n+1} \tag{14}$$

$$y_i^{n+1} = y_i^n + n_y h_i^{n+1} \tag{15}$$

where n_x, n_y are x and y components of the unit normal vector.

At the beginning and the end points of the electrode, the movement is determined by the internal angle between the electrode and the insulator. When the angle is larger than $\pi/2$, the new boundary is no longer closed in the next time step. This is physically incorrect and not logical. Obtuse angles at the interface of the electrode–insulator attract more current, hence the angle will become larger and larger as time goes on. This condition is not realistic, so no movement at these points is considered when the angle is large than $\pi/2$ (for more details about this condition, see Deconinck [12]). Therefore, movement is considered only when the internal angle between electrode and insulating boundary is equal to or less than $\pi/2$.

The new electrode profile at the first time step is closed by introducing a few elements between the new and old ends of the electrode (here two). At other time steps, the movement of the electrode is computed at every node by Equations 14 and 15. This algorithm was suggested by Deconinck [12], where a detailed description of how to deal with different cases of extremes points is reported.

The curve defining the shape of the electrode at each time step is obtained by using a uniform B-spline function. Four control points are used for each segment of a cubic B-spline and a blending function multiplies each control point coordinate accordingly [22],

$$P_i(\omega) = E_0(\omega)V_{i-1} + E_1(\omega)V_i + E_2(\omega)V_{i+1} + E_3(\omega)V_{i+2} \tag{16}$$

where P_i are the coordinates of a general point, V_i are the coordinates of the control points, E_i the blending functions, and ω a parameter varying from 0 to 1.

The four blending functions are given in the form

$$E_0(\omega) = -\omega^3/6 + \omega^2/2 - \omega/2 + 1/6 \tag{17a}$$

$$E_1(\omega) = \omega^3/2 - \omega^2 + 2/3 \tag{17b}$$

$$E_2(\omega) = -\omega^3/2 + \omega^2/2 + \omega/2 + 1/6 \tag{17c}$$

$$E_3(\omega) = \omega^3/6 \tag{17d}$$

The number of control points is two in excess of the number of interpolating points. The Yamaguchi condition is used to define an open curve (see [22] for more information), where $V_0 = V_1$ and $V_{n+1} = V_n$.

Applying Equation 16 to the interpolating points, we obtain the following linear system of algebraic equations:

$$\boldsymbol{E}\boldsymbol{V} = \boldsymbol{P} \tag{18}$$

where $\boldsymbol{E}$ is the matrix of blending functions, $\boldsymbol{V}$ is a vector of control points and $\boldsymbol{P}$ the vector of interpolating points. The problem can be solved by inverting $\boldsymbol{E}$.

The above system satisfies the Gauss–Seidel convergence condition and is more efficiently solved in an iterative way.

To compute each span we need four blending functions multiplied by four control points, but to represent the knots at the extreme of each span, one of the blending functions is zero and, consequently, we have

$$\frac{1}{6}V_{i-1}+\frac{2}{3}V_i+\frac{1}{6}V_{i+1}=P_i \quad (i=1,2,\ldots,n) \tag{19}$$

By applying the Gauss–Seidel iterative procedure, one finds

$$V_i^k=P_i+\frac{1}{2}\left\{P_i-\frac{1}{2}\left(V_{i-1}^k+V_{i+1}^{k-1}\right)\right\} \tag{20}$$

where k denotes the kth iteration. The difference vector δ_i^k between V_i^k and V_i^{k-1} may be stated as

$$\delta_i^k=P_i-V_i^{k-1}+\frac{1}{2}\left\{P_i-\frac{1}{2}\left(V_{i-1}^k+V_{i+1}^{k-1}\right)\right\} \tag{21}$$

and the iterative process continues until the difference vector be less or equal to a specified convergence tolerance. At the beginning of the process Yamaguchi suggested to use V_0^{k-1} instead of V_0^k when $i=1$ only.

The boundary elements on the curve are uniformly distributed in respect to the curve length, and their position are obtained by the use of the above B-spline functions.

In nearly all our computations the interface, after a sufficiently long time, developed a saw-toothed appearance in which the computed position of the interface points laid alternately above and below a smooth curve. This is due to the use of quadratic elements in our BEM scheme, which are known to improve the accuracy with respect to lower order elements, but in a moving boundary problem a zig-zag instability is induced as a result of the difference in accuracy between the predicted values at the end-points and those at the central node of the elements.

This stability problem was effectively controlled following the procedure described by Longuet–Higgins and Cokelet [23] to mitigate the saw-toothed appearance on the BEM results of the time evolution of space-periodic irrotational breaking waves. Longuet–Higgins and Cokelet's approach has been used successfully before in other BEM formulations of moving boundary problems [24]. The smoothing algorithm is as follows: A function $f(x)$ defined at points $x_j\,(j=1,2,\ldots)$, and in which alternate points lie on a smooth curve, can be locally approximated by two polynomials, say

$$p(x)=(a_0+a_1x+a_2x^2+\cdots+a_nx^n)+(-1)^j(b_0+b_1x+b_2x^2+\cdots+b_nx^n) \tag{22}$$

The first bracket represents a smooth mean curve, and the remainder a quantity which oscillates around the mean curve. The coefficients $a_0,a_1,\ldots$ and $b_0,b_1,\ldots$ may be chosen uniquely so that $p(x)=f(x)$ exactly at $(2n+1)$ consecutive points x_j, say $(j-n)$ to $(j+n)$ inclusive. As a smoothed function we can then take the even part:

$$p(x)=(a_0+a_1x+a_2x^2+\cdots+a_nx^n) \tag{23}$$

In the case $n=2$ this leads to the five-point smoothing formula

$$f_j=\frac{1}{16}(-f_{j-2}+4f_{j-1}+4f_{j+1}-f_{j+2}) \tag{24}$$

As the boundary shape keeps changing, the distribution of the cells in the domain also needs to be regenerated at each time step. Since the boundary shape is rarely regular, the cells cannot usually be distributed uniformly. In theory, the more irregular the boundary is, the more cells are needed to get accurate results, but too many cells could be very expensive in practical computations. To obtain the required accuracy with a minimum number of cells, an adaptive scheme was developed to automatically generate the domain mesh.

4. Numerical example

To assess the numerical approach described here, simulations are carried out on a parallel plate reactor with metal dissolution at the anode, located at the bottom of the cell, and metal deposition at the cathode, at the top of the cell (a sketch of the cell is shown in Figure 1). Electrodepositions from an electrolyte solution consisting of three ions are analyzed, in which only one ion is considered as reactive, c_1.

The current density at the two electrodes is related to electrochemical kinetics by the Butler–Volmer equation. At the anode we have:

$$J_{na}=i_a^*\left(\frac{c_1}{c_{1b}}\right)^{0.67}\left\{\exp\left[\frac{\alpha_1 nF}{RT}(V_a-U)\right]-\exp\left[\frac{-\alpha_2 nF}{RT}(V_a-U)\right]\right\} \tag{25}$$

in which α is the transfer coefficient, and at the cathode

$$J_{nc}=-i_c^*\left(\frac{c_1}{c_{1b}}\right)^{0.67}\left\{\exp\left[\frac{\alpha_1 nF}{RT}(V_c-U)\right]-\exp\left[\frac{-\alpha_2 nF}{RT}(V_c-U)\right]\right\} \tag{26}$$

where the first exponential term represents the rate of the anodic process, and the second term that of the

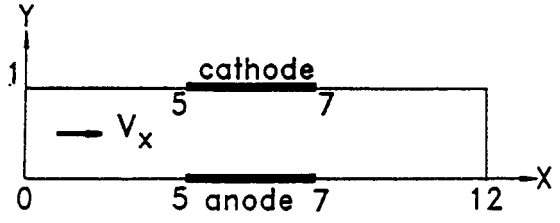

Fig. 1. Sketch of the reactor cell tested.

cathodic process. These are governed by activation energies, which depend on the surface overpotentials.

The values of the ion parameters used as input in the numerical computations are given in Table 1, where c_{0k}, with $k = 1, 2, 3$, are the incoming ion concentrations in the channel given as boundary conditions at the channel inlet, that is, $x = 0$. Table 2 gives the value of the other parameters used in our numerical examples.

The mobility constants u_k are calculated from the diffusion constants by the Nernst–Einstein formula

$$D_k = RTu_k \tag{27}$$

The following no-flux conditions were considered at the channel walls, that is, at $y = 0$ and $y = 1$, when $0 \leq x \leq 4$ and $6 \leq x \leq 12$

$$\frac{\partial c_1}{\partial n} = 0; \quad \frac{\partial c_2}{\partial n} = 0; \quad \frac{\partial c_3}{\partial n} = 0; \quad \frac{\partial U}{\partial n} = 0 \tag{28}$$

and at the channel outlet, at $x = 12$, we impose the following uniform conditions

$$\frac{\partial c_1}{\partial n} = 0; \quad \frac{\partial c_2}{\partial n} = 0; \quad \frac{\partial c_3}{\partial n} = 0; \quad \frac{\partial U}{\partial n} = 0 \tag{29}$$

At the cathode, that is, at $y = 1$, when $4 \leq x \leq 6$, the following boundary conditions were considered:

$$\frac{\partial c_2}{\partial n} = -38.6\, c_2 \frac{\partial U}{\partial n} \tag{30}$$

$$\frac{\partial c_3}{\partial n} = 77.2\, c_3 \frac{\partial U}{\partial n} \tag{31}$$

$$c_1 = c_3 - 0.5\, c_2 \tag{32}$$

$$\frac{\partial U}{\partial n} = \frac{1}{38.6(2c_1 + 0.5c_2 + 2c_3)} \times \left(\frac{0.24422}{1.3896}\right) c_1^{0.67} vexp \tag{33}$$

with

$$vexp = \exp[83.376(V_c - U)] - \exp[(-30.108)(V_c - U)]$$

Equations 30 and 31 are obtained from the zero current density condition for nonreacting ions, Equation 32 from the condition of electroneutrality, and Equation 33 from the electrochemical kinetic relation for the reactive ion, Equation 26, where

$$J_{nc} = -F^2 z_1^2 u_1 c_1 \frac{\partial U}{\partial n} - D_1 \frac{\partial c_1}{\partial n} \tag{34}$$

Table 1. Ion parameter values used in the numerical examples

k	$c_{0k} \times 10^3$/mol cm^{-3}	$D_k \times 10^5$/cm^2 s^{-1}	z_k
1	0.50	72.000	2
2	0.30	9.312	1
3	0.65	10.650	−1

Table 2. Values of other parameters used in the numerical examples

$i_a^* = i_c^* \times 10^3$ /A cm^{-2}	n	$c_{1b} \times 10^4$ /mol cm^{-3}	R /J mol^{-1} K^{-1}	T/C	α_1	α_2
1.5	2	1	8.314	25°	1.08	0.39

The normal derivative of c_1 was expressed in terms of the normal derivative of the electrical potential by using the derivative of the electroneutrality relation, and Expressions 30 and 31. Similarly at the anode, that is, at $y = 0$ when $4 \leq x \leq 6$, we have

$$\frac{\partial c_2}{\partial n} = -38.6\, c_2 \frac{\partial U}{\partial n} \tag{35}$$

$$\frac{\partial c_3}{\partial n} = 77.2\, c_3 \frac{\partial U}{\partial n} \tag{36}$$

$$c_1 = c_3 - 0.5\, c_2 \tag{37}$$

$$\frac{\partial U}{\partial n} = \frac{1}{38.6(2c_1 + 0.5c_2 + 2c_3)} \left(\frac{0.24422}{1.3896}\right) c_1^{0.67} vexp \tag{38}$$

with

$$vexp = \exp[83.376(V_a - U)] - \exp[(-30.108)(V_a - U)]$$

In the above equations the normal vector is defined outwardly to the channel.

Figure 2 shows the evolution of the cathode growth when the fluid inside the channel is at rest. These results correspond to the solution when the smoothing algorithm was used, in Figure 3 we present the results obtained without the smoothing algorithm. The corresponding current density distribution at the cathode at the beginning of the process is given in Figure 4. It is important to observe from Figure 2, that the growth at the singular points (beginning and end of the electrode) satisfies the experimental observation that the angle between the electrode and the insulator at successive time steps is a right angle (for more details about this behaviour see Deconinck [12]). Besides, due to the

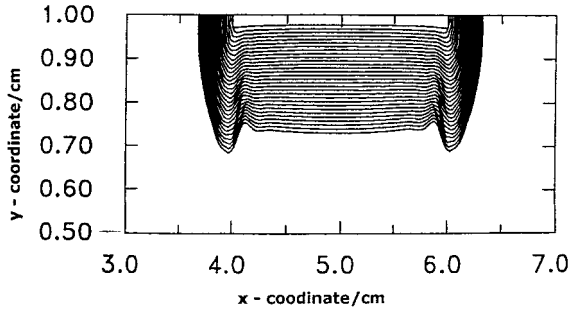

Fig. 2. Time evolution of the cathode growth in the case when the fluid inside the reactor cell is at rest, solution obtained with the smoothing algorithm.

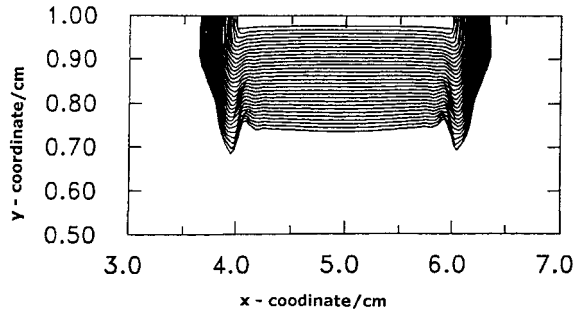

Fig. 3. Time evolution of the cathode growth in the case when the fluid inside the reactor cell is at rest, solution obtained without the smoothing algorithm.

absence of convective forces the deposition is completely symmetric.

Figures 5, 6 and 7 show how the internal cell distribution is modified as the deposition progresses, for the 2nd, 30th and the 60th time steps of the evolution, respectively. In our BEM simulation, the channel contour was divided into 38 linear boundary elements, and the shape of the internal cells was always triangular with linear interpolation. The above numerical results were allowed to grow without any physical limitation to fully appreciate the evolution of the phenomena. In practical cases when the growth material is too close to the anode an instability occurs breaking down the electrochemical process.

By comparing the present results with those obtained by Deconinck [12] using the potential model, it can be observed that when migration effects are considered, a sharper edge at the singular points i.e., the beginning and the end of the cathode, is obtained. Similar differences were observed by Deconinck [10] in some of his experimental results, which he attributed to the mass transport effect (migration), that has stronger influences at the singular points due to higher concen-

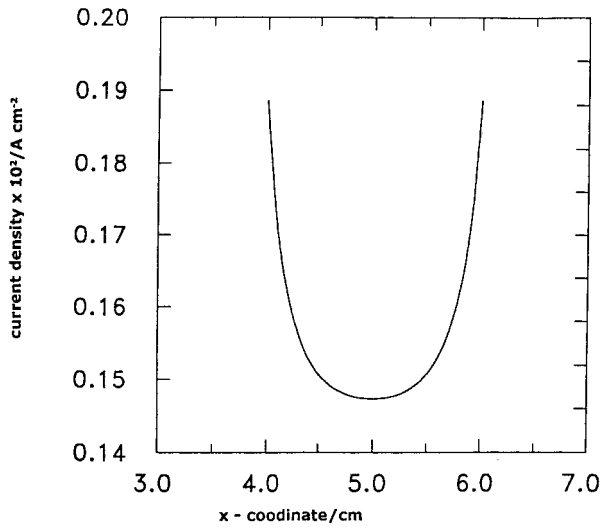

Fig. 4. Current density distribution at the cathode at the beginning of the electrodeposition process in the case when the fluid inside the reactor cell is at rest.

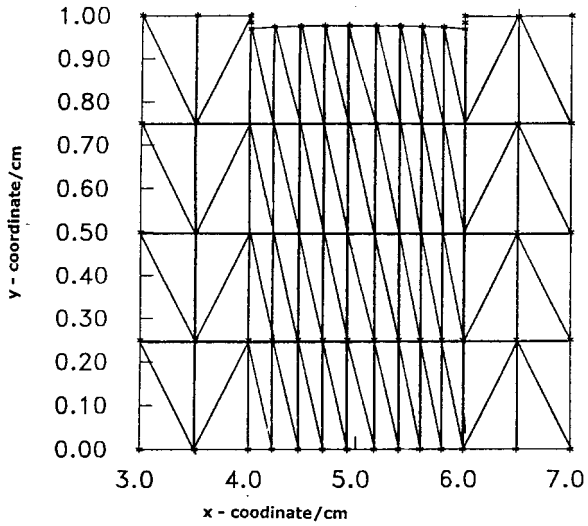

Fig. 5. Internal BEM cell distribution of the 2nd time step in the case when the fluid inside the reactor cell is at rest.

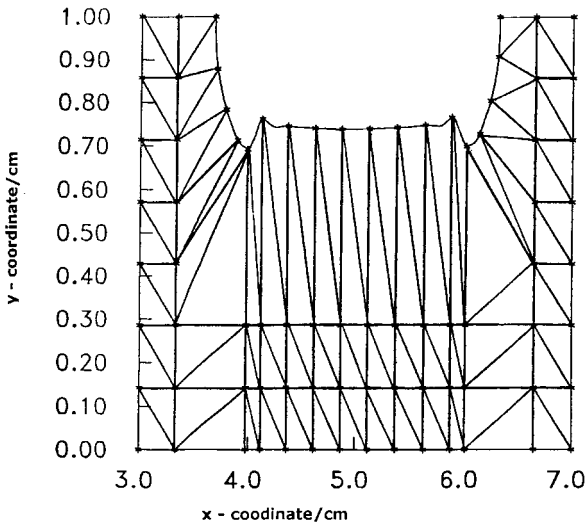

Fig. 6. Internal BEM cell distribution at the 30th time step in the case when the fluid inside the reactor cell is at rest.

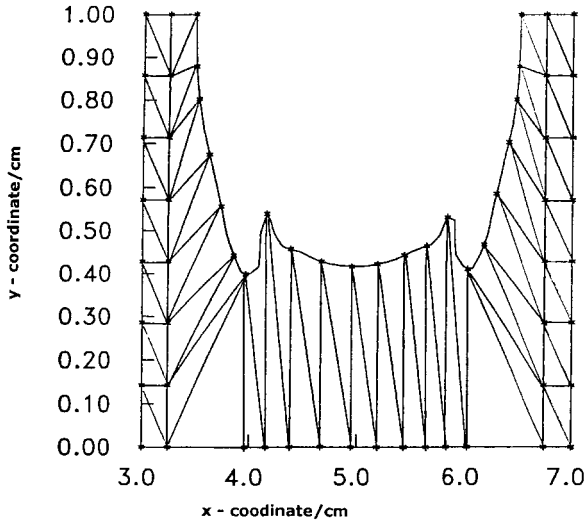

Fig. 7. Internal cell distribution at the 60th time step in the case when the fluid inside the reactor cell is at rest.

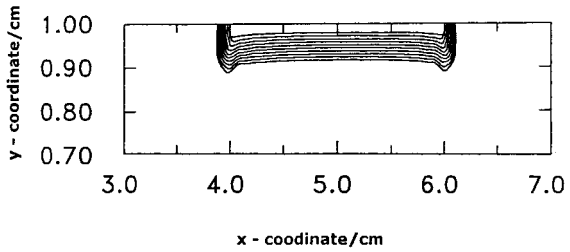

Fig. 8. Time evolution of the cathode growth for the case of convective flow and small applied voltage.

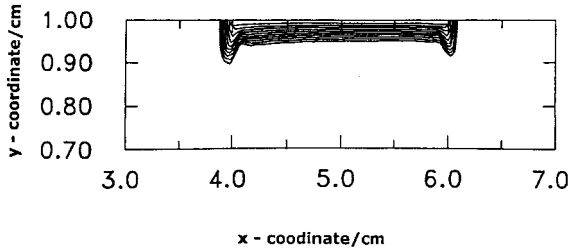

Fig. 10. Time evolution of the cathode growth for the case of convective flow and moderate applied voltage.

tration gradients there. The migration effect was not considered in his simulations.

Besides the above difference between the results obtained with a potential model and the ones presented here, it is also expected that the present approach will predict nonsymmetric depositions when fluid convection is present, as shown in the next examples. In a potential model the current distribution has to be independent of the flow rate, since convection is large enough to eliminate concentration variations, and therefore the current distribution predicted by this type of model and the concurrent electrodeposition have to be symmetric.

Figures 8, 10 and 12 show the results obtained in the case of an initial laminar parabolic channel flow, with an initial cross section Péclet number ($Pe_k = v_{\max}h/D_k$), $Pe_1 = 26.85$, $Pe_2 = 347.20$ and $Pe_3 = 2347$, for different values of the applied voltage. When the magnitude of the applied electrical voltage is low (30 mV), the resulting deposition profile is practically uniform having two small humps, at the beginning and at the end of the cathode, of almost equal sizes (Figure 8). In Figure 9, we show the corresponding current density distribution at the cathode at the beginning of the process. By increasing the magnitude of the applied electrical voltage to 45 mV, while keeping the same convective flow field, it is found that the deposition surface shows a small slope towards the upstream direction of the channel, and the hump at the beginning becomes larger than the one at the end (Figure 10). In Figure 11 we present the corresponding current density distribution at the beginning of the process, for this cell conditions.

When the applied voltage was increased to such a value that the limiting current density condition was reached, the deposition reduces practically to a single hump at the beginning of the cathode (Figure 12). In this condition it is possible to neglect the contribution of ionic migration to the flux of the reacting ions leading to a pure convective diffusion phenomena. Frequently, due to the small value of the diffusion coefficient, the concentrations differ significantly from the bulk values only in a thin layer near the surface of the electrode, where the parabolic velocity profile can be approximated by a linear function. For this condition Léveque [25] found an approximate analytical solution, in which the current density decreases with the inverse cube root of the distance downstream of the cathode. In Figure 13, we present the comparison of our initial current density with that obtained with Léveque's formula for the flow conditions of this last example.

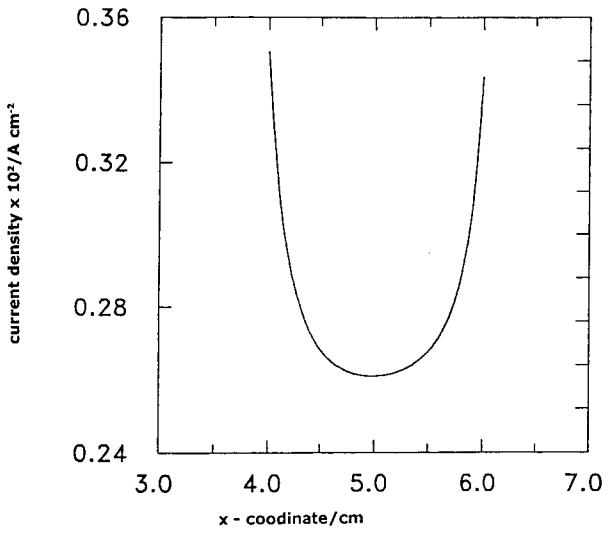

Fig. 9. Current density distribution at the cathode at the beginning of the electrodeposition process for the case of convective flow and small applied voltage.

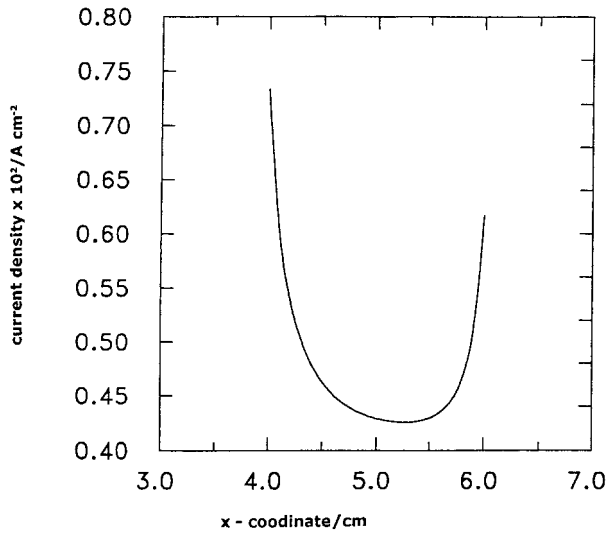

Fig. 11. Current density distribution at the cathode at the beginning of the electrodeposition process for the case of convective flow and moderate applied voltage.

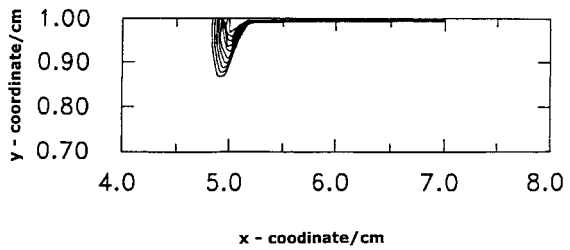

Fig. 12. Time evolution of the cathode growth for the case of convective flow at limiting current density condition.

It is important to observe that, for simplicity, we have assumed that the velocity profile remains parabolic during the deposition process. But as the deposition progresses, the velocity profile is modified at each cross section according to the conservation of mass. Therefore, our solutions are expected to hold at the beginning of the deposition process, when fluid flow separation is negligible.

Finally, it is interesting to observe the similarity between the different electrode shapes obtained in this work, and the shapes of the bed forms found at the bottom of alluvial channels produced by the motion of the sediments, which are carried out by the main fluid. A general classification of those bed forms is: ripples, dunes, wavy bed, transition flat bed and antidunes. These bed features will appear according to different flow intensities and sediment characteristics (for more details see Raudkivi [26]). The present numerical results show similar variations on the electrodeposition patterns when the ratio between the intensity of the convective flow and the applied electrical voltage changes. A major difference between these two phenomena is that in the sediment transport process, the decantation force (the gravitational force) is one-dimensional, and is unaffected by the other fields. However, in the present electrodeposition process the attracting force, due to the electrical potential, is two-dimensional and influenced by the presence of the other fields.

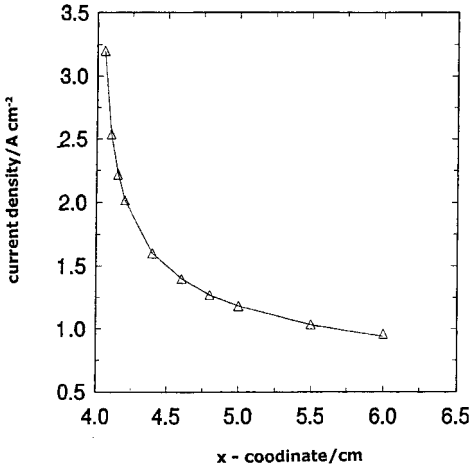

Fig. 13. Current density distribution at the cathode at the beginning of the electrodeposition process for the case of convective flow at the limiting current density condition.

Conclusion

By changing the relative magnitude of the acting forces in an electrochemical decomposition process, the corresponding changes on the deposition patterns have been numerically observed. These go from complete symmetric features, when the fluid is at rest, to an almost single hump deposition at the beginning of the cathode when the limiting current condition is reached. These patterns can be found in electrochemical experiments and they appear according to the differences in magnitude between the convective term and the attractive force due to the chemical reaction at the electrode. An almost uniform deposition is observed when convection is considered and a small electrical voltage is applied, and unsymmetric deposition is found when the supply of the reaction solution is not enough to ensure symmetric growth for both extremes of the electrode.

Acknowledgements

This work forms part of the Brite–Euram project BE-5187, funded by the European Commission. The authors would like to thank the reviewers of the Journal of Applied Electrochemistry for their helpful suggestions.

References

1. T.A. Witten and L.M. Sander, *Phys. Rev. Lett.* **47** (1981) 1400.
2. T.A. Witten and L.M. Sander, *Phys. Rev. B.* **27** (1983) 5686.
3. D.A. Haslebeck, PhD thesis, University of California, San Diego (1989).
4. Kwok Yue-Kuen and C.C.K. Wu, *Comput. Methods Appl. Mech. Eng.* **132** (1996) 305.
5. M.M. Menon and U. Landau, *J. Electrochem. Soc.* **134**(9) (1987) 2248.
6. E.K. Yung and L.T. Romankiv, *J. Electrochem. Soc.* **136**(3) (1989) 756.
7. Z.H. Qiu, L.C. Wrobel and H. Power, *J. Eng. Anal. Boundary Elements* **15** (1995) 299.
8. Z.H. Qiu, L.C. Wrobel and H. Power, *J. Appl. Electrochem.* **27** (1997) 1333.
9. S. Das and A.K. Mitra, *Int. J. Num. Meth. Eng.* **35** (1992) 1045.
10. J. Deconinck, PhD thesis, Vrije Universiteit, Brussel (1985).
11. J. Deconinck, G. Maggetto and J. Vereecken, *J. Electrochem. Soc.* **132** (1985) 2960.
12. J. Deconinck, *J. Appl. Electrochem.* **24** (1994) 212.
13. J.O. Dukovic, IBM *J. Res. Dev.* **34** (1990) 693.
14. G.A. Prentice and C.W. Tobias, *J. Electrochem. Soc.* **129** (1982) 72.
15. W. Huang and D.B. Hibbert, *Am. Math. Soc.* **16** (1995) 270.
16. W. Huang and D.B. Hibbert, *Phys. Rev. E* **53** (1996) 727.
17. A. Calusaru, *Rev. Chem. Bucuresti* **8** (1957) 369.
18. A. Calusaru, 'Electrodeposition of Metal Powders, Materials Sciences Monographs', 3 (1979).
19. I. Atanasia and A. Calusaru, *Studii Cercet. Met. Bucharest* **2** (1957) 237.
20. M.G. Pavlovic, S. Kindlova and I. Rousar, *Electrochim. Acta* **37**(1) (1992) 23.

21. J. Newman, 'Electrochemical Systems', 2nd edn (Prentice-Hall, Englewood Cliffs, NJ, 1991).
22. J.J.S.P. Cabral, PhD thesis, Wessex Institute of Technology, UK (1992).
23. M.S. Longuet-Higgins and E.D. Cokelet, *Proc. R. Soc. Lond.* **A350** (1976) 1.
24. K.X.H. Zhao, H. Power and L.C. Wrobel, *J. Eng. Anal. Boundary Elements* **19** (1997) 331.
25. M.A. Léveque, *Annales des Mines* **12** (1928) 201.
26. A.J. Raudkivi, 'Loose Boundary Hydraulics' (Pergamon Press, Oxford, 1976).